

Unveiling the Supercapacitive Performance of B, P Dual-Doped Graphene in Triple Redox Additives

S. Suresh Balaji,^[a] V. Vignesh,^[a] and A. Pandurangan^{*[a]}

Dual heteroatom doping of graphene is currently presumed as more promising for energy storage applications. In addition, the development of energy density with multiple redox additives is paying special attention. Here, we report the fabrication of B, P dual-doped graphene in three various weight combinations. The formation and the quantity of the prepared samples were investigated by XRD, FT-IR, EDAX and XPS. The B, P dual-doped graphene derived from the weight ratio of boron and phosphorus dopant in 1:3 has achieved an enriched gravimetric

capacitance of 360 F g^{-1} at 1 A g^{-1} ($1 \text{ M H}_2\text{SO}_4$) and greater than RGO (151 F g^{-1}). The energy density of the fabricated symmetric supercapacitor cell is found to be 50 Wh kg^{-1} in triple redox additives in $1 \text{ M H}_2\text{SO}_4$ solution which is greater than KI (33 Wh kg^{-1}) and $1 \text{ M H}_2\text{SO}_4$ alone (5 Wh kg^{-1}) at 2 A g^{-1} . Also, the same cell delivered an increased stability of 99.7% of capacitance retained from its initial value after 7000 charge-discharge cycles at 5 A g^{-1} .

1. Introduction

Because of the speedy rise of energy demand and immense fuel consumption, the development of research based on renewable fuel gathered serious attention. To satisfy the essential needs for renewable energy, the development of energy storage devices with user as well as environmentally friendly, inexpensive and enriched performance is highly warranted.^[1] Supercapacitors are preferred due to their multi-various advantages such as enhanced power density, fast charging-discharging rate, prolonged electrochemical stability, and convenient assembly in all-solid-state devices.^[2] Due to the discrimination in the mechanism of charge storage process and the electrodes, supercapacitors are detached into two groups namely Electrochemical double-layer capacitors (EDLC) and Pseudocapacitors (PC).^[3] EDLC materials include activated carbon, aerogel, Graphene, porous carbon, CNFs, and CNTs and involve purely non-faradaic charge storage behavior.^[4-8] The pseudocapacitive electrode materials typically involve fast redox processes and comprise transition element-based sulfides, oxides and hydroxides, MOF systems, and conducting polymer.^[9-21] However, the latter category suffers serious pitfall arising out of feeble stability due to the variation in the crystallinity, phase, and the extent of hydration upon cycling stability.^[22] This necessitates using EDLC-based carbon materials for supercapacitor devices that deliver excellent stability.

Among the variety of carbon materials, graphene has been explored extensively due to its excellent credits such as enhanced specific surface area, high electrical conductivity, and improved thermal stability.^[23] Yet the unescapable restacking

within the sheets of graphene is presumed to be disadvantageous for the energy storage performance due to the feeble exposure of surface area that impedes the access of ions over the electrode. Thus, the reliable solution to sort out this issue is the substitution of heteroatoms into graphene lattice via doping. It has been well established that doping the graphene with a variety of heteroatoms such as N, S, B, and P could improve the electrochemical performance.^[24] Moreover, the dual doping of heteroatoms over graphene is expected to enrich the charge storage behavior through the synergistic effect of two different heteroatoms.^[25] Yu et al. developed the P, S co-doped graphene via pyrolysis between phytic acid and thioglycolic acid at 900°C under an inert atmosphere for 2 h and attained the specific capacitance of 438 F g^{-1} at 10 mV s^{-1} in $1 \text{ M H}_2\text{SO}_4$.^[26] Duraisamy Prakash et al. fabricated the B, N co-doped graphene via hydrothermal using ammonia and boric acid as the precursors at 90°C about 12 h and delivered the enhanced specific capacitance of 885 F g^{-1} at 1 A g^{-1} in 6 M KOH solution.^[27] Kong et al. prepared the N, S co-doped graphene by hydrothermal treatment of GO with ammonium thiocyanate at 180°C for 8 h and achieved the enriched specific capacitance of 320 F g^{-1} at 1 A g^{-1} in 6 M KOH solution.^[28] Wang et al. obtained the dual N, S co-doped graphene by electrophoresis technique treating the required quantities of GO with ammonia and polystyrene sulfonate for 2 h accompanied by the in-situ microwave treatment and achieved the gravimetric capacitance of 354 F g^{-1} at 0.5 A g^{-1} in $1 \text{ M Et}_4\text{NBF}_4$ acetonitrile electrolyte via three-electrode system.^[29] Li et al. developed the N, P co-doped graphene with a hydrothermal route using various mass ratios of GO and ammonium dihydrogen phosphate and accomplished the specific capacitance of 348 F g^{-1} at 1 A g^{-1} in 6 M KOH aqueous solution.^[30] Sim et al. obtained the N and F co-doped graphene quantum dots via CVD followed by the subsequent plasma treatment and delivered the specific capacitance of 244 F g^{-1} at 3 A g^{-1} in 1 M KOH solution.^[31] Chen et al. developed the N, F dual doped holey graphene via hydrothermal processing and attained the

[a] S. Suresh Balaji, V. Vignesh, A. Pandurangan

Department of Chemistry, Anna University, Chennai – 600 025, Tamil Nadu, India

E-mail: pandurangan_a@yahoo.com

 Supporting information for this article is available on the WWW under <https://doi.org/10.1002/batt.202400021>

gravimetric capacitance of 345.4 F g^{-1} at 1 A g^{-1} in 6 M KOH aqueous solution.^[32] Sandhiya et al. prepared the crumpled B, P co-doped graphene nanosheets via supercritical fluid technique with 3-fluorobenzene boronic acid as the dopant at 400°C for 1 h involving the different weight ratios of GO and precursor and demonstrated the enriched specific capacitance of 506 F g^{-1} at 1 A g^{-1} in 1 M H_2SO_4 electrolyte.^[33] Besides, we also explored the multiple heteroatom-doped graphene for electrochemical energy storage applications.^[34–36]

The most essential task in the carbon-based symmetric supercapacitor is the improvement of energy density which can be executed by either improving the capacitance via incorporating the redox-mediated species or increasing the operating voltage with non-aqueous or ionic liquid electrolytes. However, the latter route suffers serious limitations such as the expensive, use of advanced glove boxes and specially designed cell so-called Swagelok cells. Furthermore, the stability of the device is not attractive. To furnish an appropriate remedy, redox additive components are preferred because they raise the charge storage behavior by enriching the pseudocapacitance of the working electrode as a result of redox processes that happened between the electrolyte ions and the redox species.^[37–39] Besides, the use of glove boxes and Swagelok cells are not at all required which permits the researchers to give more priority to the aqueous-based redox species instead of non-aqueous as well as ionic liquid electrolytes. Interestingly, the redox additives species are further explored for all-solid-state flexible device applications which substantiates the strong role of redox additives in improving the energy density of carbon-based symmetric supercapacitors.^[40–42] SenthilKumar et al. studied the supercapacitive performance of porous activated carbon in VOSO_4 /1 M H_2SO_4 achieving the capacitance of 630.6 F g^{-1} at 1 mA cm^{-2} which is higher than 1 M H_2SO_4 solution.^[43] Karnan et al. demonstrated that a significant improvement in energy density for the biodevived porous carbon was observed upon the incorporation of hydroquinone (HQ) as a redox additive.^[44,45] Recently, dual redox components have been explored for enhancing the energy density of carbon-based symmetric supercapacitors. Arul Raja et al. reported that the energy density of manganese ammonium phosphate with graphene quantum dots is enhanced by 1.6-fold after incorporating the dual redox additive mixture such as KI and VOSO_4 .^[46] In addition, many reports about the development of energy density with dual redox mixtures are available.^[47–51] Here we report for the first time the use of triple redox additives for the significant development towards the energy density of fabricated symmetric supercapacitor cells. In this work, we have synthesized the B, P dual doped graphene in three various weight combinations and the one in which the boron and phosphorus dopants are in a 1:3 weight ratio achieved the enriched gravimetric capacitance of 360 F g^{-1} at 1 A g^{-1} in 1 M H_2SO_4 solution which is relatively higher than RGO (151 F g^{-1}) by three-electrode experiments. Also, the full-cell investigations revealed that the energy density of the assembled symmetric supercapacitor cell was found to be 50 Wh Kg^{-1} at 2 A g^{-1} in triple redox additives involving potassium iodide (KI), hydroquinone (HQ) and potassium ferricyanide ($\text{K}_3[\text{Fe}(\text{CN})_6]$) which is

superior to $0.01 \text{ M KI}/1 \text{ M H}_2\text{SO}_4$ (33 Wh Kg^{-1}) and 1 M H_2SO_4 (5 Wh Kg^{-1}), respectively. All electrochemical experiments were performed with techniques such as cyclic voltammetry (CV) and galvanostatic charge-discharge (GCD).

Experimental Section

Synthesis of B, P Dual-Doped Graphene

The graphene oxide (GO) was synthesized by modified Hummer's method and the RGO was synthesized by hydrothermal treatment of GO at 200°C for 24 h. Three different B, P dual-doped graphene samples are prepared by treating sodium phosphate and boric acid with graphene oxide in which the dopant of boron and phosphorus are in the weight ratio of 1:3, 1:1, and 3:1 under hydrothermal condition with Teflon-lined autoclave at 200°C for 24 h are denoted as B1P3GO, BPGO, and B3P1GO, respectively. In addition, the B and P singly doped materials are prepared by the hydrothermal treatment of GO with appropriate precursors in a 1:1 weight proportion under the same experimental conditions. The complete experimental procedure for the preparation of GO is indicated in the supplementary information.

Materials Characterization

Instruments used for the materials characterization and electrochemical characterization of prepared materials are specified in the supplementary material.

2. Results and Discussion

The existence of the two prominent peaks in which a wide peak near $2\theta = 25^\circ$ for the (002) plane and a minor peak at $2\theta = 44^\circ$ for the (100) plane are observed in the XRD pattern of B1P3GO, BPGO, B3P1GO, and RGO as revealed from Figure 1a. This suggests that the graphene oxide was reduced by the hydrothermal reaction of GO with precursors of boron and phosphorus at 200°C for 24 h.^[35] Raman spectra of B1P3GO, BPGO, B3P1GO and RGO are shown in Figure 1b which comprises a couple of well-defined absorption bands. The band that occurred at 1350 cm^{-1} denotes the D band and another one that existed at 1590 cm^{-1} symbolizes the G band.^[52] The D band is termed as a defective band that labels the multivarious defects like hydroxy group, epoxy group, carbonyl groups, dangling bonds, phenolic groups, and sp^3 hybridized carbon.^[53] Another important G band named as graphitic band specifies the Brillouin zone with doubly degenerated E_{2g} phonons and chiefly deduces the olefinic character of carbon materials from which the extent of graphitization could be predicted with I_D/I_G value.^[52] From the four various samples, the I_D/I_G value of RGO is the lowest which suggests that the B, P co-doped/functionalized graphene has received more defects when compared with RGO. It was observed that the I_D/I_G value increases when the content of phosphorus precursor increases. This might be attributed to the fact that the P–O functionalities would generate more defects compared to boron-bonded groups. Both the XRD pattern and Raman spectra of BGO and PGO are

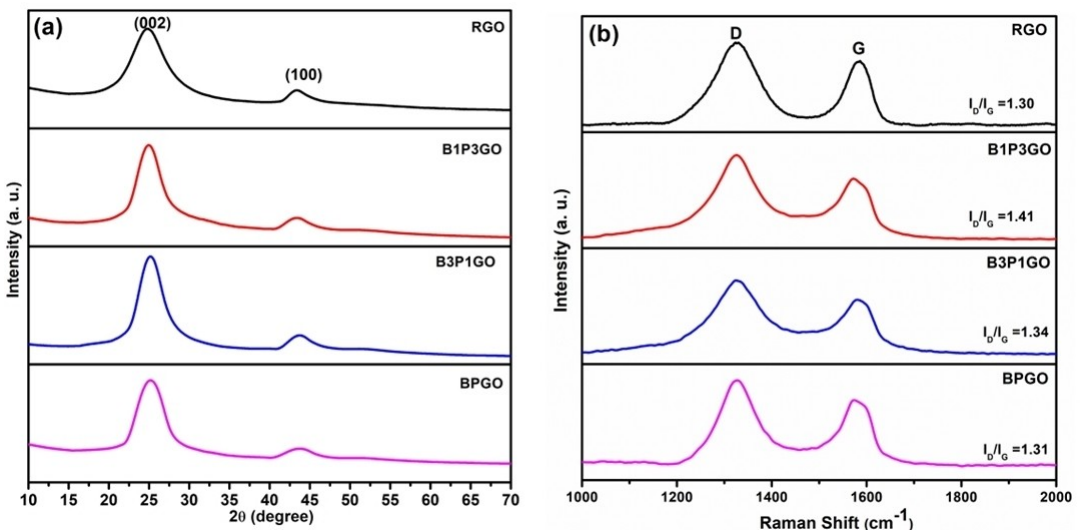


Figure 1. (a) XRD pattern and (b) Raman spectra of B1P3GO, BPGO, B3P1GO and RGO.

displayed in Figures S1a and b, respectively. From Figure S1b, the I_D/I_G value of BGO is higher than PGO implying that the boron-oxygen created more defects compared to phosphorus functionalities.

FT-IR spectrum of B1P3GO, B3P1GO and BPGO is exhibited in Figure 2. In all three samples, the bands that appeared around 1114, 1385, and 1620 cm^{-1} are attributed to B-C or P-O, antisymmetric B-O stretching, and C=O stretching, respectively. In the FT-IR spectrum of B3P1GO, bands observed around 1120 and 1156 cm^{-1} are attributed to B-C stretching.^[54] Additionally, another set of bands around 1233 and 1308 cm^{-1} are ascribed to B-C stretching, respectively.^[55] The existence of the B-O bond is recognized by the appearance of a couple of

bands at 1382 and 1455 cm^{-1} are ascribed to antisymmetric B-O stretching.^[56]

X-ray photoelectron spectroscopy was used to validate the nature of doped atoms over the carbon matrix. XPS survey spectrum of B1P3GO is exhibited in Figure S2. The atomic percentage of boron, phosphorus, carbon and oxygen from the survey spectrum is estimated to be about 0.38, 0.69, 84.97 and 13.96 at.%, respectively. XPS deconvoluted B1s, P2p and C1s spectrum of B1P3GO are exhibited in Figure 3a, b and c, respectively. The pair of binding energies at 191.8 and 197.7 eV are attributed to $\text{BC}_3/\text{O}-\text{BC}_2$ and C- BO_2 , respectively. In general, higher binding energy values are associated with the boron atoms being multiply bonded with high electronegative atoms and agree with the earlier report.^[57] Next for the high-resolution P2p spectrum as shown in Figure 3b, the existence of binding energy at 133.4 and 134.5 revealed the presence of P-C and P-O bonds, respectively.^[58] It is essential to indicate that the intensity of the P-C bond is higher than the P-O bond implying that the phosphorus atom is doped into the graphene network. From Figure 3c, the presence of binding energy at 284.2, 285.6 and 288.7 eV indicated the variety of groups such as C=C, C-P/C-B and C=O, respectively.^[59] Among the three, the intensity of C=C is higher suggesting the presence of olefinic carbon atoms from the graphene network.

Figure 4 depicts the HRSEM images of B1P3GO, BPGO and B3P1GO. Here the graphene sheets are arranged one over the other and also crumpled. This kind of sheet-like morphology is advantageous for electrochemical energy storage applications. The elemental composition of B1P3GO BPGO, B3P1GO, BGO and PGO are identified from the EDAX spectrum which is displayed in Figure S3. The atomic contents of carbon, oxygen, boron and phosphorus of these five samples are listed in Table S1. Moreover, the graphene sheets are distributed from HRTEM images as displayed in Figure 5.

The BET N_2 adsorption-desorption isotherm and the BJH pore size distribution profile for B1P3GO, B3P1GO and BPGO are

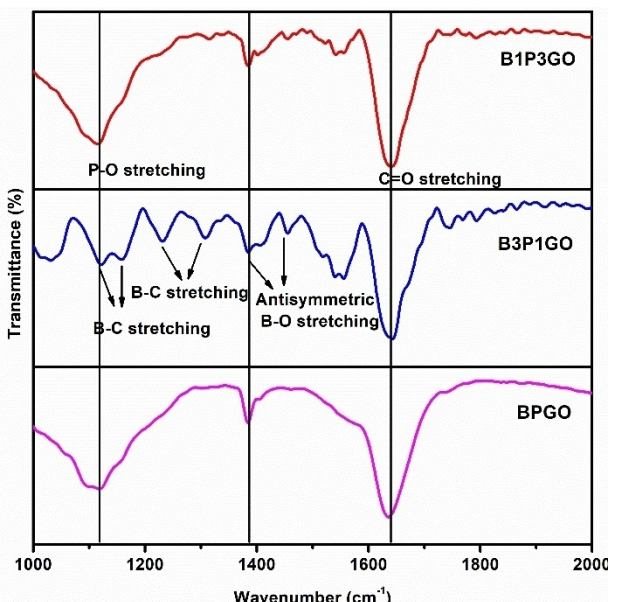


Figure 2. FT-IR spectra of B1P3GO, BPGO and B3P1GO.

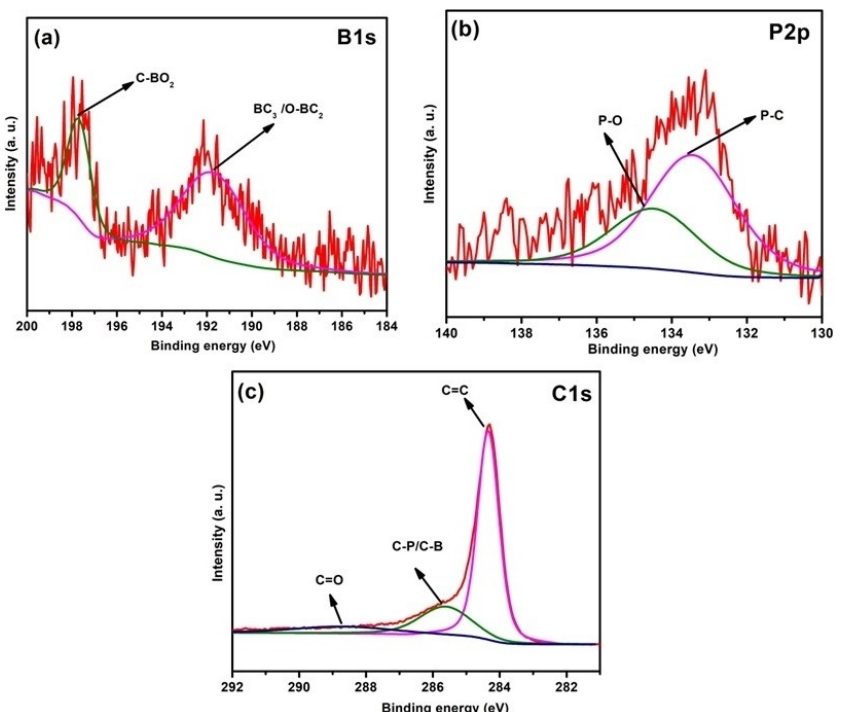


Figure 3. High-resolution XPS spectrum of (a) B1s, (b) P2p, and (c) C1s spectrum of B1P3GO.

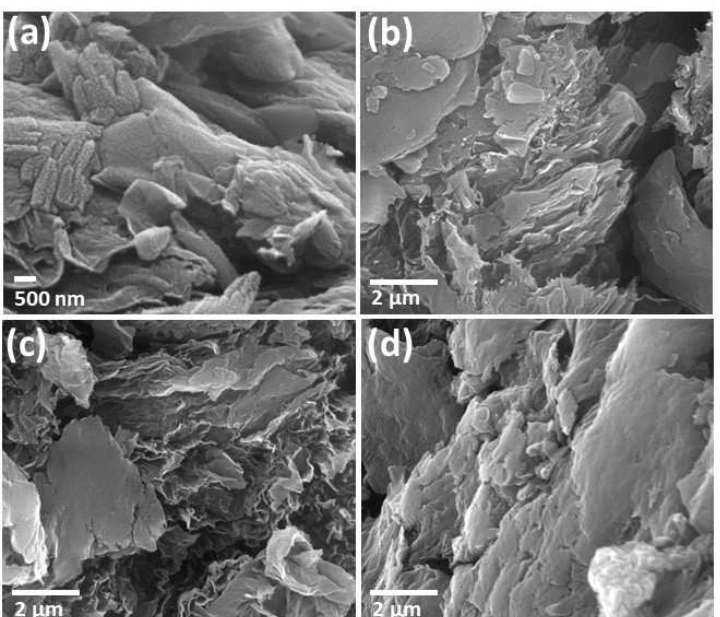


Figure 4. High-resolution SEM images of (a) and, (b) B1P3GO, (c) B3P1GO and (d) BPGO.

exhibited in Figures 6a and b, respectively. The calculated value of S_{BET} from Figure 6a for B1P3GO, B3P1GO and BPGO are found to be 187.13, 158.5 and 127.6 $\text{m}^2 \text{g}^{-1}$, respectively. Also, Figure 6a revealed the type II adsorption isotherm. The values of specific surface area, pore volume and pore diameter determined from the BJH pore size distribution profile for B1P3GO, B3P1GO and BPGO are specified in Table 1. From the three

Table 1. Pore volume and Pore diameter for B1P3GO, BPGO and B3P1GO.

Samples	Pore volume (cc/g)	Pore diameter (nm)	$S_{\text{BET}}(\text{m}^2 \text{g}^{-1})$
B1P3GO	0.243	3.541	187.13
B3P1GO	0.233	3.524	158.5
BPGO	0.191	3.531	127.6

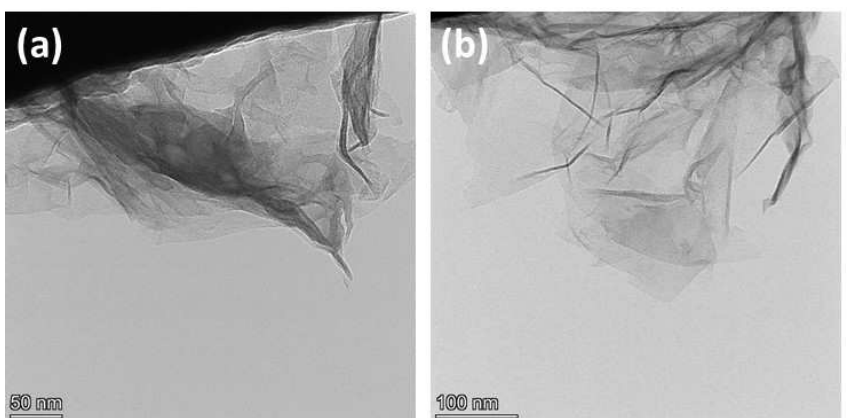


Figure 5. High-resolution TEM images of (a) and, (b) B1P3GO.

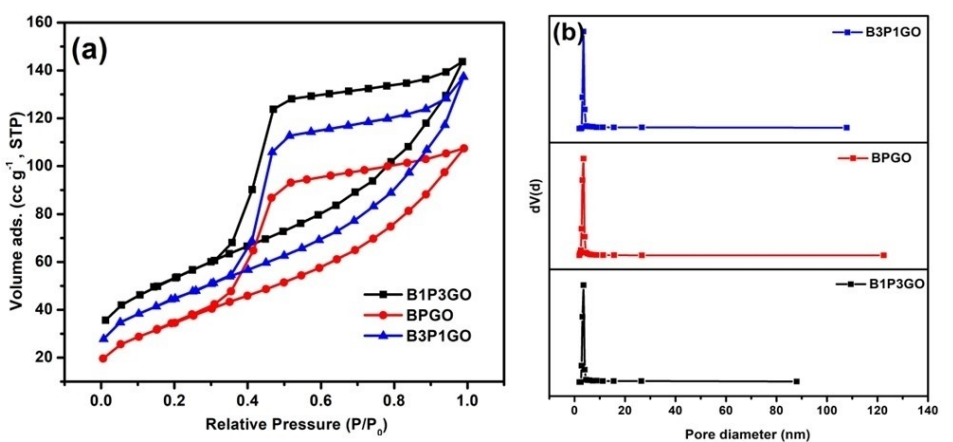


Figure 6. (a) BET N_2 adsorption–desorption profile and (b) pore size distribution profile for B1P3GO, B3P1GO and BPGO.

samples, the B1P3GO has got the maximum S_{BET} and pore volume.

To investigate the capacitance of B1P3GO, BPGO and B3P1GO, both CV and GCD were performed in 1 M H_2SO_4 as the electrolyte. Figures 7a and b depicts the CV and GCD profile of B1P3GO, BPGO and B3P1GO at 5 mVs⁻¹ and 1 Ag⁻¹ in 1 M H_2SO_4 solution. From Figure 7a, the area under the CV curve is more pronounced for the B1P3GO electrode and also the existence of a broad redox peak in the CV profile validates the pseudocapacitance of the electrode occurring as a result of electrochemical interaction between the doped heteroatoms and ions of the electrolyte.^[33] Among the three electrode materials, the discharge time is higher for the B1P3GO electrode suggesting that it possesses the enhanced charge storage

behavior. The order of gravimetric capacitance ($F\text{ g}^{-1}$) is B1P3GO (360) > B3P1GO (265) > BPGO (221) and agrees with those of S_{BET} and pore volume determined from Figure 6. Hence it has been interpreted that the enhanced S_{BET} might be the plausible reason for the increased capacitance by the B1P3GO. Both Figures 7c and d represent the CV and the GCD profile for the B1P3GO electrode at different scan rates and current densities, respectively. The broadness in the CV profile is too observed even at a high scan rate. Besides, the faintly distorted GCD profile symbolizes the redox behavior of B, P co-doped graphene in an acidic electrolyte. The gravimetric capacitance of B1P3GO, BPGO and B3P1GO at various current densities are tabulated in Table 2. Based on Table 2, the rate capability calculated for the B1P3GO, BPGO and B3P1GO at 5 Ag⁻¹ is

Table 2. The gravimetric capacitance of B1P3GO, BPGO and B3P1GO from the GCD profile at different current densities.

Samples	Specific Capacitance ($F\text{ g}^{-1}$)					
	1 Ag^{-1}	2 Ag^{-1}	3 Ag^{-1}	4 Ag^{-1}	5 Ag^{-1}	10 Ag^{-1}
B1P3GO	360	325	289	265	250	200
BPGO	221	163	113	70	38	
B3P1GO	265	210	169	145	125	75

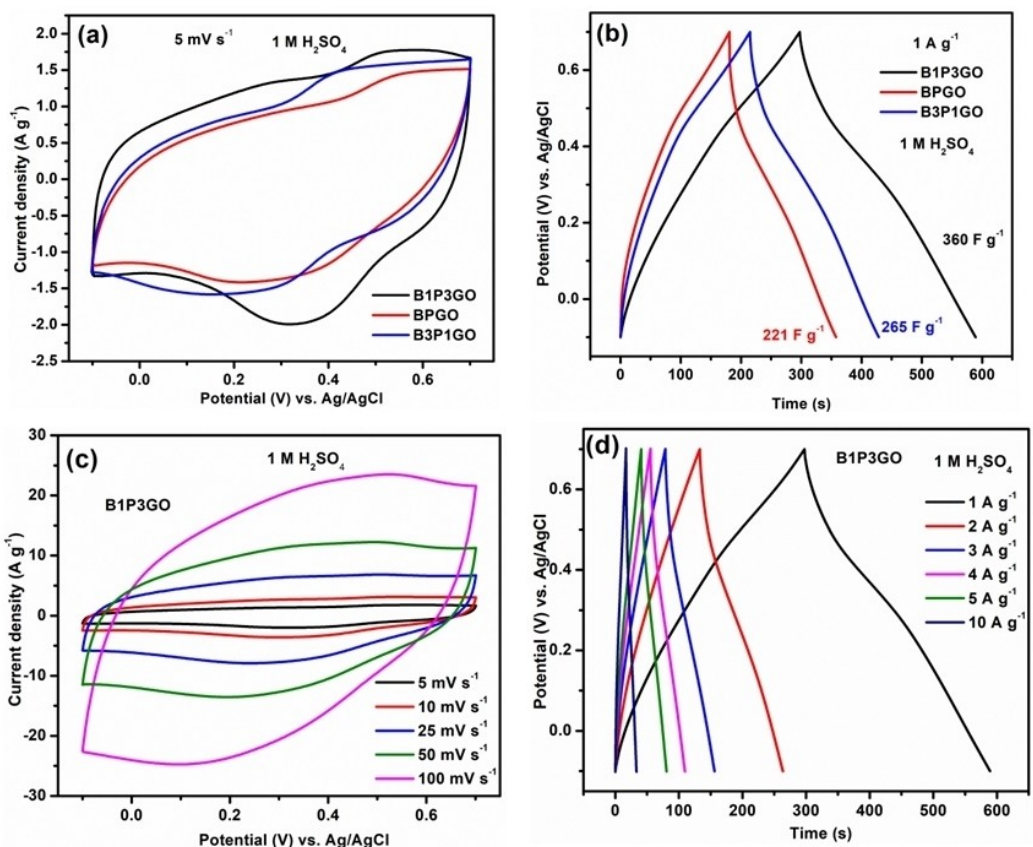


Figure 7. (a) CV and (b) GCD profile of B1P3GO, BPGO and B3P1GO in 1 M H_2SO_4 solution at 5 mV s^{-1} and 1 A g^{-1} , (c) CV and (d) GCD profile of B1P3GO in 1 M H_2SO_4 solution at different scan rates and different current densities, respectively.

found to be 69%, 17% and 47%, respectively. Hence it has been suggested that both the gravimetric capacitance and the rate capability obey the same sequence.

To realize the impact of co-doping over graphene network for energy storage applications, the electrochemical performance of B, P co-doped graphene was compared with that of B and P individually doped graphene and RGO. Both CV and GCD profiles of B1P3GO, BGO, PGO and RGO at 5 mV s^{-1} and 1 A g^{-1} in 1 M H_2SO_4 solution are displayed in Figure 8a and b, respectively. Among the four electrode materials, the current density from the CV profile is higher for the B1P3GO electrode as evident from Figure 8a. This was also further confirmed from the GCD profile (Figure 8b) that the discharge duration of the B1P3GO electrode is relatively higher compared to other electrodes. Hence it has been proposed that the dual doping of heteroatom over graphene lattice played a substantial role by improving the capacitance. From Figure 8c, the calculated rate capability of B1P3GO, BGO, PGO and RGO are found to be 69%, 43%, 59% and 49% at 5 A g^{-1} suggesting that the B1P3GO electrode is superior to other electrodes in terms of both capacitance and rate capability. Hence it has been inferred that the dual atom doping over graphene framework is highly essential for improving the energy storage performance. The capacitance of B, P dual-doped graphene obtained in this work is compared with other dual heteroatom-doped graphene reported in previous literature and tabulated in Table 3. The

Electrochemical Impedance spectroscopy (EIS) was recorded for the B1P3GO, B3P1GO and BPGO in the frequency range of 100 KHz to 10 mHz and displayed in Figure S4. The charge transfer resistance (R_{ct}) calculated for the B1P3GO, B3P1GO and BPGO are found to be 0.37, 0.42 and 0.38Ω , respectively. It has been suggested that the lower the charge transfer resistance of the electrode, the higher the conductivity of the electrode. At the low-frequency region, the slope of the line parallel to the y-axis is steeper for the B1P3GO electrode implying that it possesses the perfect capacitive behavior.

To explore the charge storage property of B1P3GO as a symmetric supercapacitor in aqueous medium, the symmetric supercapacitor cell is assembled by placing the two B1P3GO electrodes having the same loading in a cell with 1 M H_2SO_4 solution. Figures 9a and b show the CV and GCD profile of B1P3GO-based symmetric supercapacitors with varying cell voltages from 0.7 to 1 V at 50 mV s^{-1} and 1 A g^{-1} , respectively. The gravimetric capacitance of the B1P3GO symmetric supercapacitor at 0.7, 0.8, 0.9 and 1 V are found to be $166, 170, 178$ and 184 F g^{-1} , respectively. It was inferred that the optimized cell voltage for a doped graphene-based symmetric supercapacitor is 1 V and agrees well with the earlier report.^[68] It was demonstrated that the capacitance for the symmetric cell rises with cell voltage. Figures 9c and d reveal the CV and GCD curves for the symmetric B1P3GO cell at different scan rates and current densities, respectively. The typical carbon-based

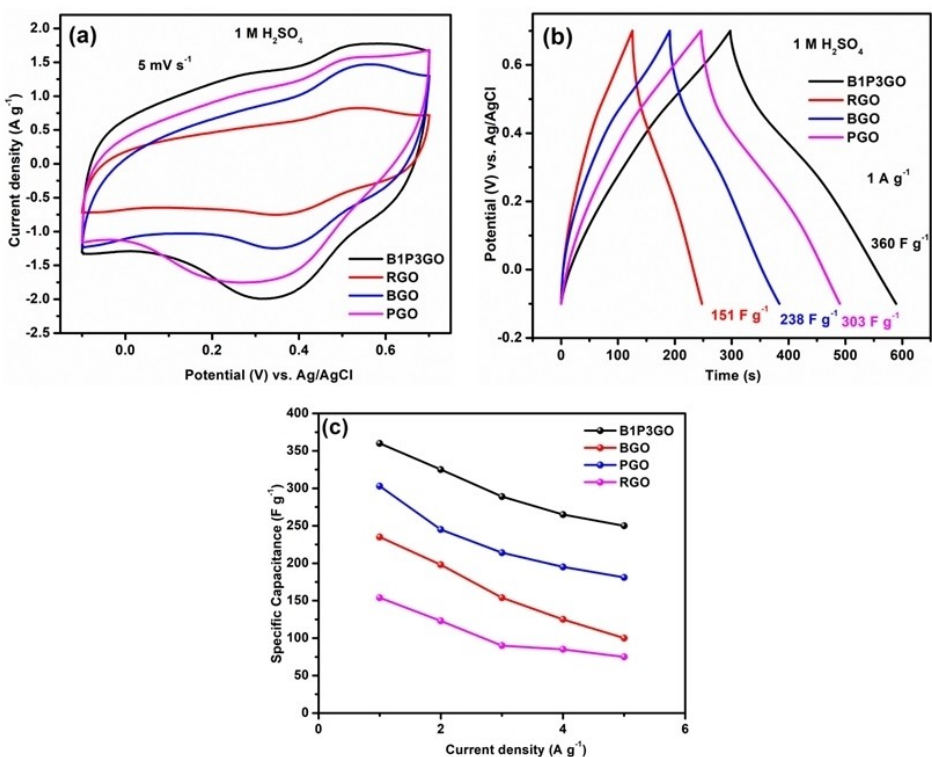


Figure 8. (a) CV and (b) GCD profile of B1P3GO, BGO, PGO and RGO in 1 M H_2SO_4 solution at 5 mV s^{-1} and 1 A g^{-1} , (c) Plot of specific capacitance versus current density for B1P3GO, BGO, PGO and RGO.

symmetric capacitor is recognized with triangular GCD and rectangular CV profile.

Both Figures S5a and b represent the CV and GCD profiles for the B1P3GO and RGO-based symmetric supercapacitors in 1 M H_2SO_4 solution. From Figure S5b, the calculated specific capacitance of B1P3GO-based symmetric cell at 1 A g^{-1} is found to be 184 F g^{-1} which is higher than RGO (112 F g^{-1}) implying that the presence of dual doped heteroatoms made a significant improvement towards the capacitance. From Figure S5c, the calculated rate capability for the B1P3GO-based

symmetric supercapacitor at 10 A g^{-1} is found to be 32% which is relatively higher than RGO (14%) implying that the presence of doped heteroatoms enhances the retention rate of capacitance.

It has been reported extensively in the literature that the charge storage performance for any carbon-based materials is amplified to a greater extent with the incorporation of redox additives in aqueous electrolytes.^[56] Both CV and GCD profiles for the B1P3GO electrode in 0.01 M KI, 0.01 M $\text{K}_3[\text{Fe}(\text{CN})_6]$ and 0.01 M HQ in 1M H_2SO_4 solution are exhibited in Figure 10a and

Table 3. Comparison of the gravimetric capacitance of B, P dual doped graphene obtained in this work with other heteroatom doped graphene reported in the different kinds of literature.

Materials	Precursors	C_{sp} (F g^{-1})	Electrolyte	Ref.
B, N co-doped graphene	Melamine diborate	130.7 F g^{-1} @0.2 A g^{-1}	1 M H_2SO_4	[60]
B, N co-doped graphene	Polyaspartamide and benzene-1,4-diboronic acid	284 F g^{-1} @1 A g^{-1}	2 M KOH	[61]
B, N co-doped graphene	1-butyl-3-methylimidazolium tetrafluoroborate	133.6 F g^{-1} @0.5 A g^{-1}	1 M H_2SO_4	[62]
B, N co-doped graphene	Boric acid and ammonia solution	885 F g^{-1} @1 A g^{-1}	6 M KOH	[27]
N, S co-doped graphene	Thiocarbohydrazide	141 F g^{-1} @0.3 A g^{-1}	6 M KOH	[63]
N, S co-doped graphene	Ammonium thiocyanate	320 F g^{-1} @1 A g^{-1}	6 M KOH	[28]
N, P co-doped graphene	Ammonium dihydrogen phosphate	348 F g^{-1} @1 A g^{-1}	6 M KOH	[30]
N, P co-doped graphene	Ammonium dihydrogen phosphate	320 F g^{-1} @1 A g^{-1}	1 M H_2SO_4	[64]
N, F co-doped graphene	Melamine and PTFE	230 F g^{-1} @0.5 A g^{-1}	6 M KOH	[65]
N, I co-doped graphene	Potassium iodide and ammonium iodide	268 F g^{-1} @1 A g^{-1}	6 M KOH	[66]
N, Se co-doped graphene	Urea and diphenyl selenide	302.9 F g^{-1} @1 A g^{-1}	6 M KOH	[67]
B, P dual-doped graphene	Boric acid and sodium phosphate	360 F g^{-1} @1 A g^{-1}	1 M H_2SO_4	This work

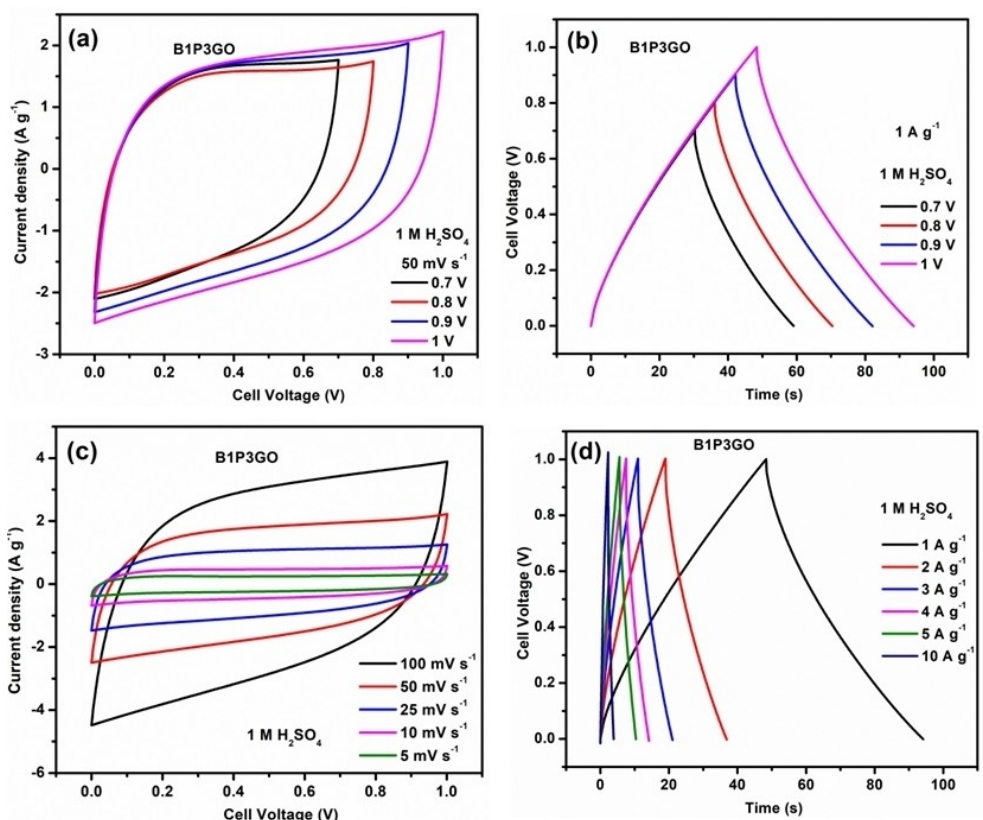
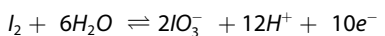
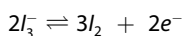
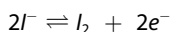
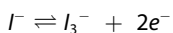


Figure 9. (a) CV and (b) GCD profile of B1P3GO symmetric cell at 50 mV s⁻¹ and 1 A g⁻¹, (c) CV and (d) GCD profile of B1P3GO symmetric cell at different scan rates and current densities, respectively.

b, respectively. The appearance of redox peaks in the CV profile is attributed to the faradaic reactions from the electrolyte to the redox-mediated species. However, the peak potentials are different for different redox additives. Among these, the area enclosed by the CV curve is the maximum for the hydroquinone and the redox peak that appeared around between 0.41 and 0.54 V is attributed to the faradaic transformation of quinone to hydroquinone. From Figure 10b, the calculated value of the capacitance for the B1P3GO electrode is found to be 736 F g⁻¹ at 3 A g⁻¹ which is highest for the KI redox additive compared to other redox-mediated compounds. The sequence of redox processes responsible for the interaction between KI and H₂SO₄ is depicted as shown below^[69]



Because of the above sequence of redox reactions influenced by the KI as a redox additive that involves the transition of I from -1 (I⁻) to 0 (I₂) and from 0 (I₂) to +5 (IO₃⁻), the charge storage performance of the B1P3GO is enhanced to a larger extent compared to other redox additives such as HQ and

K₃[Fe(CN)₆]. Figures 10c and d show the CV and GCD profile for the B1P3GO electrode in 0.01 M KI/1 M H₂SO₄ at different scan rates and current densities. The electrochemical reversibility of the electrode with KI as a redox additive is easily identified in Figure 10c. The existence of peaks at 0.33, 0.45, 0.24 and 0.39 V in the CV profile of B1P3GO electrode in 0.01 M KI/1 M H₂SO₄ at 5 mV s⁻¹ are labelled as OP1, OP2, RP1 and RP2, respectively. They are associated with faradaic processes of KI in acidic electrolytes and also the peak potential changes with scan rate as observed in Figure 10c. The specific capacitance of the B1P3GO electrode in 0.01 M KI/1 M H₂SO₄ at varying current densities such as 3, 6, 8 and 10 A g⁻¹ are found to be 739, 589, 524 and 482 F g⁻¹, respectively. The specific capacitance of the B1P3GO electrode with different redox additives is shown in Table 4. The CV and GCD profiles for both B1P3GO and RGO electrodes at 5 mV s⁻¹ and 3 A g⁻¹ are displayed in Figure 11a

Table 4. The gravimetric capacitance of B1P3GO in 0.01 M KI, 0.01 M K₃[Fe(CN)₆] and 0.01 M HQ in 1 M H₂SO₄ aqueous solution from the GCD profile at different current densities.

Redox Additives	Specific Capacitance (F g ⁻¹)			
	3 A g ⁻¹	6 A g ⁻¹	8 A g ⁻¹	10 A g ⁻¹
KI	739	589	524	482
K ₃ [Fe(CN) ₆]	567	507	458	409
HQ	513	475	444	418

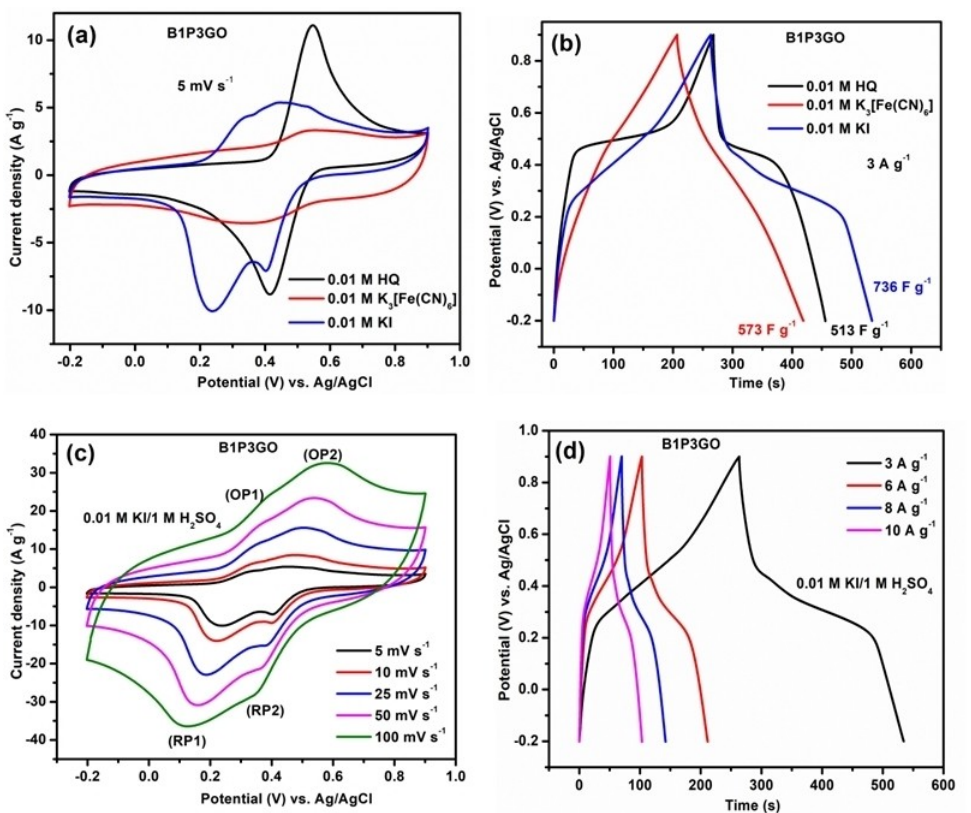


Figure 10. (a) CV and (b) GCD profile of B1P3GO in 0.01 M KI, 0.01 M K₃[Fe(CN)₆] and 0.01 M HQ in 1 M H₂SO₄ solution at 5 mV s⁻¹ and 3 A g⁻¹, (c) CV and (d) CD profile of B1P3GO in 0.01 M KI–1 M H₂SO₄ solution at different scan rates and current densities, respectively.

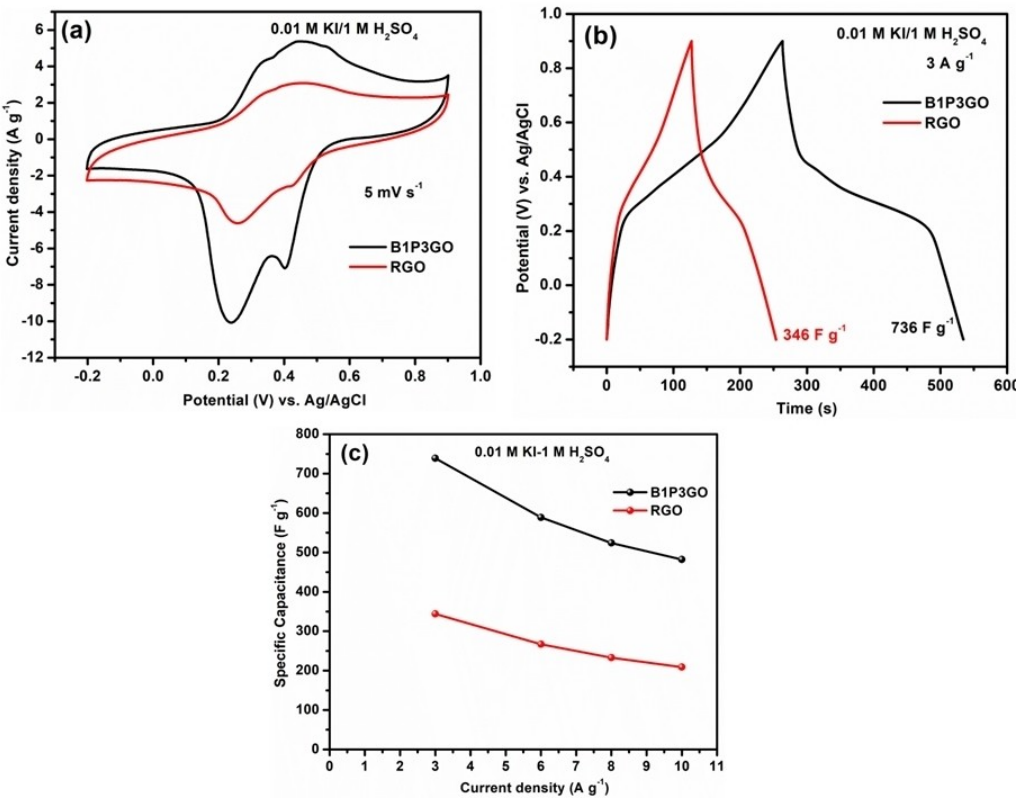


Figure 11. (a) CV and (b) GCD profile of B1P3GO and RGO at 5 mV s⁻¹ and 3 A g⁻¹, (c) Rate performance profile for both B1P3GO and RGO in 0.01 M KI in 1 M H₂SO₄ solution at different current densities.

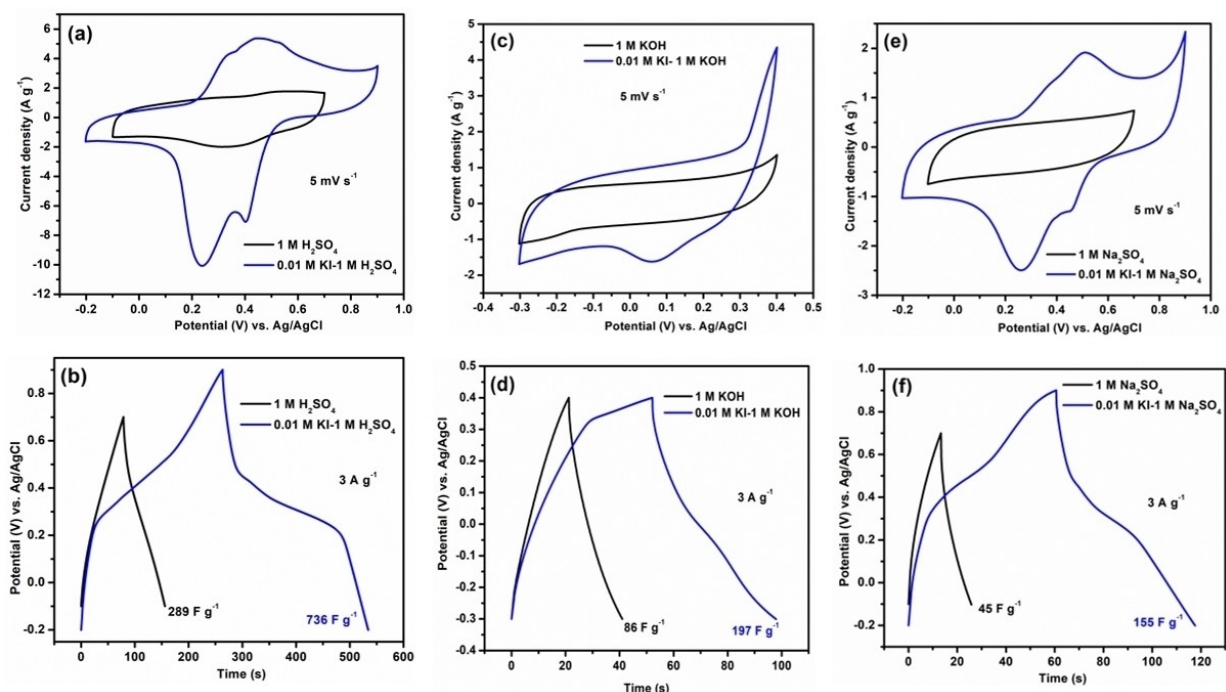


Figure 12. (a) CV and (b) GCD profile of B1P3GO in 1 M H_2SO_4 solution and 0.01 M KI, in 1 M H_2SO_4 solution, (c) CV and (d) GCD profile of B1P3GO in 1 M KOH and 0.01 M KI-1 M KOH solution and (e) CV and (f) GCD profile of B1P3GO in 1 M Na_2SO_4 solution and 0.01 M KI in 1 M Na_2SO_4 solution at 5 mV s⁻¹ and 3 A g⁻¹, respectively.

and b, respectively. The current density for the B1P3GO electrode is higher than RGO as shown in Figure 11a. The calculated gravimetric capacitance of the B1P3GO electrode from Figure 11b is found to be 736 F g⁻¹ which is superior to RGO (346 F g⁻¹). The gravimetric capacitance corresponding to both B1P3GO and RGO electrodes are plotted against different current densities and shown in Figure 11c. The rate performance for the B1P3GO electrode is found to be 65% which is faintly higher than RGO (61%) implying that the doped heteroatoms did not create an impact on the capacitance retention in redox additive-based electrolytes.

To appreciate the influence of the medium, the electrochemical supercapacitive performance of the B1P3GO electrode was studied in three different media (1 M H_2SO_4 , 1 M KOH and 1 M Na_2SO_4) with and without redox additive. The CV and GCD profiles of the B1P3GO electrode in 1 M H_2SO_4 , 1 M KOH and 1 M Na_2SO_4 in the presence and absence of redox additive (KI) are displayed in Figures 12 a-f. The presence of rectangular kind of CV and triangular type of GCD in 1 M KOH and 1 M Na_2SO_4 suggests that the EDLC behavior of the B1P3GO electrode is more prominent in alkaline and neutral medium where the adsorption of H^+ ions towards the electrode surface is nil and consistent with previous report.^[70] This implied that the doped heteroatoms are electrochemically inert in alkaline and neutral media but highly active in an acidic medium. Hence, the order of gravimetric capacitance (F g⁻¹) at 3 A g⁻¹ calculated for the B1P3GO electrode from Figure 12b, d and f are 289 (1 M H_2SO_4) > 86 (1 M KOH) > 45 (1 M Na_2SO_4). The value of the specific capacitance of B1P3GO in various media at different current densities is tabulated in Table S2. The trend in

the order of gravimetric capacitance is also the same for the redox additive. From Figures 12a, b and c, the redox behavior of the KI over the B1P3GO electrode is more predominant in 1 M H_2SO_4 and 1 M Na_2SO_4 while such kind of redox interactions are not reflected in the CV profile when carried out in 1 M KOH solution. The possible cause might be attributed to which both I^- and OH^- are electron-rich and may not permit the redox processes of KI to occur in an alkaline medium. Therefore, it was clearly understood that the charge storage performance in redox additives is also strongly influenced by the nature of the media. The values of the specific capacitance of B1P3GO in acidic, alkaline and neutral media with redox additive (KI) are tabulated in Table 5.

It was generally presumed that if the pseudocapacitance behavior enhances then the capacitance value too rises. Both CV and GCD profile of the B1P3GO electrode in 0.01 M KI/1 M H_2SO_4 and the mixture of 0.01 M KI, 0.01 M HQ and 0.01 M $\text{K}_3[\text{Fe}(\text{CN})_6]$ (triple redox additives)/1 M H_2SO_4 are displayed in Figure 13 a and b, respectively. From Figure 13b, it was found

Table 5. The gravimetric capacitance of B1P3GO in 1 M H_2SO_4 , 1 M KOH and 1 M Na_2SO_4 in 0.01 M KI from the GCD profile at different current densities.

Redox Additives	Specific Capacitance (F g ⁻¹)			
	3 A g ⁻¹	6 A g ⁻¹	8 A g ⁻¹	10 A g ⁻¹
1 M H_2SO_4 /0.01 M KI	739	589	524	482
1 M KOH/0.01 M KI	197	120	91	71
1 M Na_2SO_4 /0.01 M KI	155	98	80	64

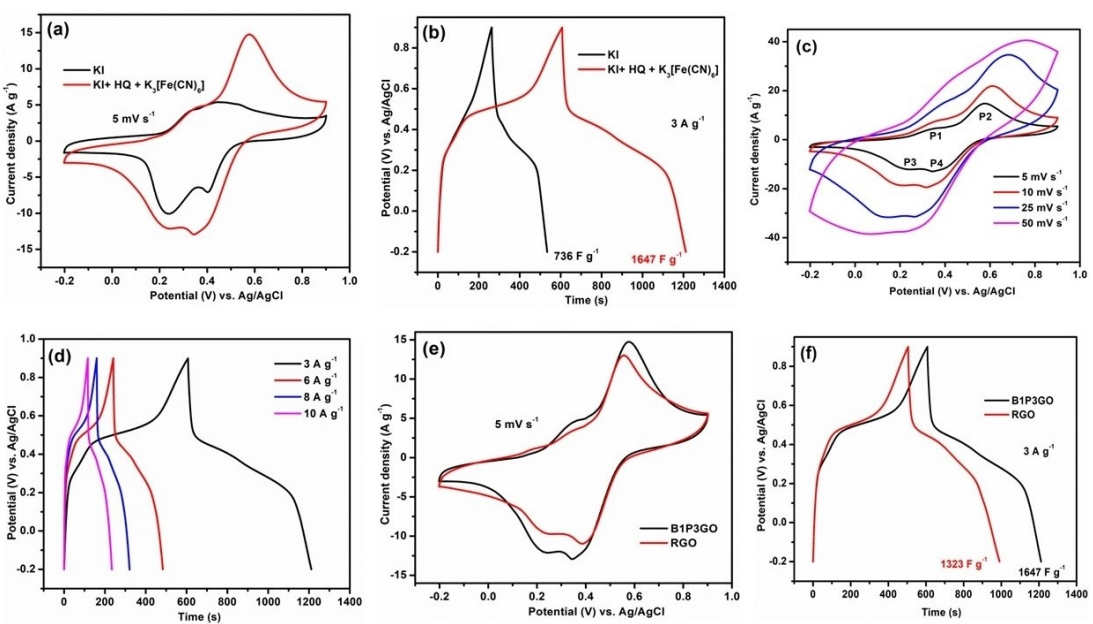


Figure 13. (a) CV and (b) GCD profile of B1P3GO in 0.01 M KI in 1 M H_2SO_4 solution and 0.01 M KI, 0.01 M HQ and 0.01 M $\text{K}_3[\text{Fe}(\text{CN})_6]$ in 1 M H_2SO_4 solution, (c) CV and (d) GCD profile of B1P3GO at varying scan rates and current densities, (e) CV and (f) GCD profile of B1P3GO and RGO in 0.01 M KI, 0.01 M HQ and 0.01 M $\text{K}_3[\text{Fe}(\text{CN})_6]$ in 1 M H_2SO_4 solution at 5 mV s^{-1} and 3 Ag^{-1} , respectively.

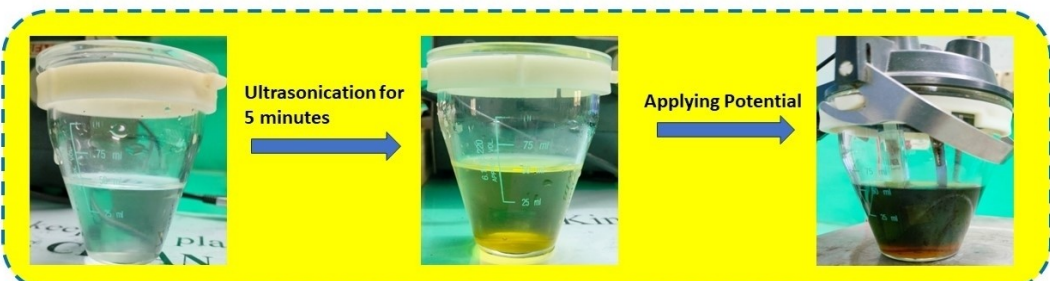
that the gravimetric capacitance of the B1P3GO electrode in 0.01 M KI is found to be 736 F g^{-1} at 3 Ag^{-1} which is 2.2-fold lower than the triple redox additive (1647 F g^{-1}). The CV and the GCD for the B1P3GO in triple redox additives with varying scan rates and current densities are shown in Figure 13 c and d, respectively. When the scan rate is enhanced, then the shape of redox peaks in the CV profile gets distorted. This implied that the redox processes within the redox additives and the acidic electrolyte are more efficient at a low scan rate. The amplified performance is attributed to the combined pseudocapacitance by the triple redox additives. From Figure 13c, the four peaks at 0.34, 0.57, 0.24 and 0.34 V are designated as P1, P2, P3 and P4, respectively. All four peaks are associated with redox processes within the redox additive mixtures and H_2SO_4 . To differentiate the performance of the B1P3GO electrode from the RGO, the CV and GCD were performed for both RGO and the B1P3GO and displayed in Figure 13 e and f, respectively. The calculated specific capacitance of the RGO electrode in triple redox additives is found to be 1323 F g^{-1} which is slightly lower

compared to the B1P3GO electrode (1647 F g^{-1}) at 3 Ag^{-1} advising that the doped heteroatoms exhibited the slightly higher capacitance over the RGO even in triple redox additives. The scheme for the color change of the electrochemical cell containing triple redox additives in acidic electrolytes is shown in Scheme 1.

To envisage whether the nature of adsorption of ions via either diffusion or capacitive mechanism, the logarithmic relationship between peak current and scan rate was investigated for all the observed anodic and cathodic peaks in cyclic voltammogram of the B1P3GO electrode in all the three distinguishable redox additives at multiple scan rates and the mathematical expression is represented below^[71]

$$i = av^\beta \quad (1)$$

Where i , v and β stand for the current, scan rate, and arbitrary constant, respectively. Figures 14a, b and c depict the logarithmic plot of scan rate dependence on current for the



Scheme 1. Variation of the color of the electrochemical cell containing electrolyte upon the addition of triple redox additives.

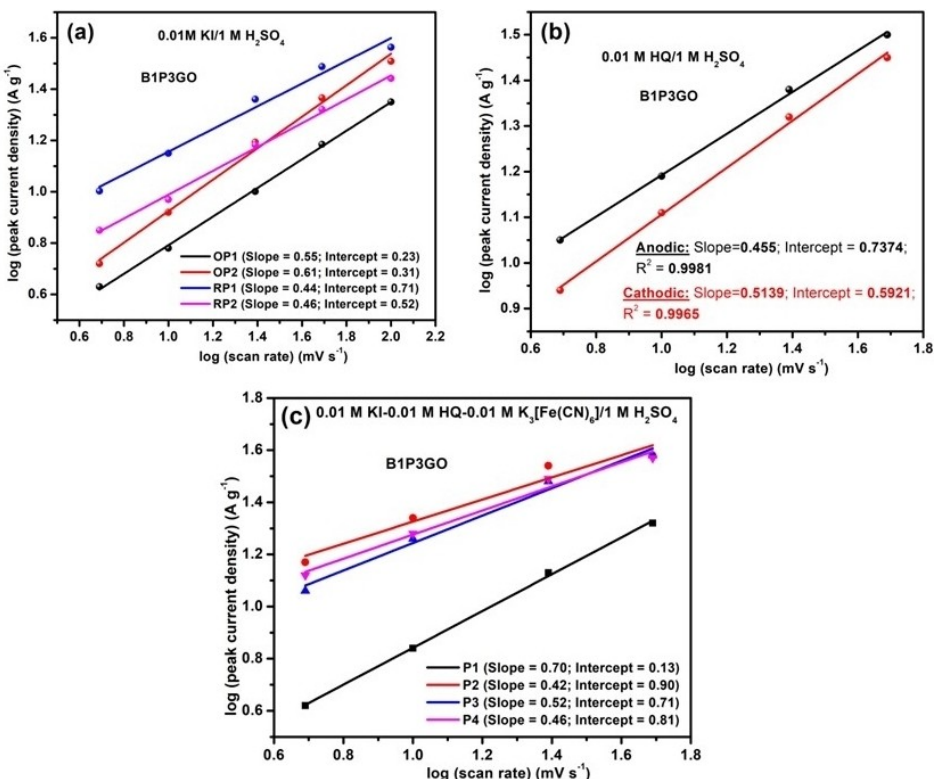


Figure 14. Plot of logarithmic peak current against scan rate for the B1P3GO electrode in (a) KI, (b) HQ and (c) triple redox additives.

B1P3GO electrode in KI, HQ, and triple redox additives. On taking the linear fit of the plot for all three redox additives, the value of the slope is observed to be closer to 0.5 implying that the charge storage reactions associated with all the reversible redox peaks are diffusion-controlled.

The percentage of contribution of EDLC and pseudocapacitance of the B1P3GO electrode in all the three redox additive electrolytes (KI, HQ, and triple redox additives) are determined using the Trasatti method analysis and corresponding graphs are displayed in Figure S6 a-f. The detailed procedure of the Trasatti method of analysis is elaborated in Supporting Information ESI. The bar diagram of the specific capacity of the B1P3GO electrode material with the contribution of the EDLC (red) and PC (blue) is exhibited in Figure S7.

Figure 15a and b represent the CV and GCD profile for the symmetric B1P3GO cell in 0.01 M KI-1 M H_2SO_4 with varying cell voltages from 1 to 1.7 V at 50 mV s^{-1} and 3 A g^{-1} , respectively. Normally, the permissible limit of cell voltage for any carbon-based symmetric supercapacitor in aqueous electrolytes is around 1.2 V. However, it was demonstrated that the humps appeared in the CV profile when performed after 1.2 V suggesting that the faradaic processes between the redox species and electrolyte ions are prominent after the potential for the electrochemical decomposition of water (1.23 V). From Figure 15b, the calculated value of specific capacitance for the B1P3GO-based symmetric cell at varying voltages such as 1, 1.1, 1.2, 1.3, 1.4, 1.5, 1.6 and 1.7 V are found to be 204, 218, 220, 222, 231, 240, 248 and 261 F g^{-1} , respectively. Thus, the optimized working voltage is 1.7 V because the maximum

gravimetric capacitance is attained at this voltage. Both CV as well as GCD profiles for the symmetric B1P3GO cell at several scan rates and current densities are displayed in Figure 15 c and d, respectively. The calculated gravimetric capacitance of symmetric B1P3GO cells at current densities such as 2, 3, 4, 6, 8 and 10 A g^{-1} are found to be 325, 268, 226, 184, 151 and 132 F g^{-1} , respectively. Besides, the rate capability of the B1P3GO symmetric cell is calculated to be $40.6\% @ 10 \text{ A g}^{-1}$ proposing that the charge storage due to faradaic reactions is severely suppressed at high current density.

To enhance the energy density further, the electrochemical capacitance for the symmetric B1P3GO cell was studied in triple redox additives (KI-HQ-K₃[Fe(CN)₆]) in 1 M H_2SO_4 . The CV and GCD profile for the symmetric B1P3GO cell in 0.01 M KI, 0.01 M HQ and 0.01 M K₃[Fe(CN)₆]-1 M H_2SO_4 with varying cell voltages from 1 to 1.7 V at 50 mV s^{-1} and 3 A g^{-1} are exhibited in Figure S8 a and b, respectively. Both CV and GCD profiles for the symmetric B1P3GO cell at 5 mV s^{-1} and 2 A g^{-1} were shown in Figures 16 a and b. The appearance of redox humps around 0.2–0.4 V in the symmetric B1P3GO cell is contributed by the redox reactions associated with hydroquinone and potassium ferricyanide while such redox humps are not observed for the same cell where KI is the only redox additive. From Figure 16b, the calculated gravimetric capacitance and the energy density at 2 A g^{-1} for the B1P3GO symmetric cell in triple redox additives (KI-HQ-K₃[Fe(CN)₆]) are found to be 494 F g^{-1} and 50 Wh Kg^{-1} which are 1.47 times greater than that in KI delivering the values of gravimetric capacitance and energy density as 334 F g^{-1} and 33 Wh Kg^{-1} , respectively. Figures 16c

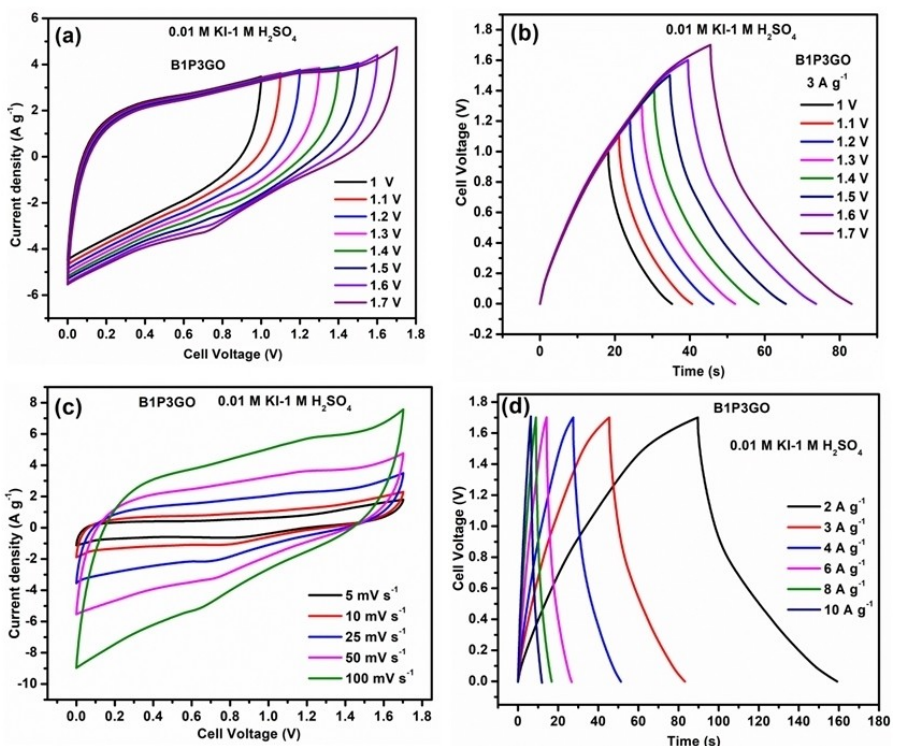


Figure 15. (a) CV and (b) GCD profile of B1P3GO symmetric cell at 50 mV s^{-1} and 3 A g^{-1} at different cell voltages, (c) CV and (d) GCD profile of B1P3GO symmetric cell at different scan rates and current densities in $0.01 \text{ M KI-1 M H}_2\text{SO}_4$ solution, respectively.

and d present the CV and GCD profile for the B1P3GO symmetric cell at a variety of scan rates and current densities, respectively. The redox humps are not seen in the CV curve at a higher scan rate implying that the rate of faradaic processes associated with redox additive and the electrolyte is so fast at a higher scan rate. From Figure 16d, the rate capability for this

symmetric cell at 10 A g^{-1} is found to be 43% suggesting that the rate of retention of capacitance is deteriorated due to strong redox processes influenced by the three distinguishable redox additives. The electrochemical stability of the B1P3GO symmetric cell in triple redox additives was analyzed by carrying out the continuous GCD over 7000 cycles at 5 A g^{-1}

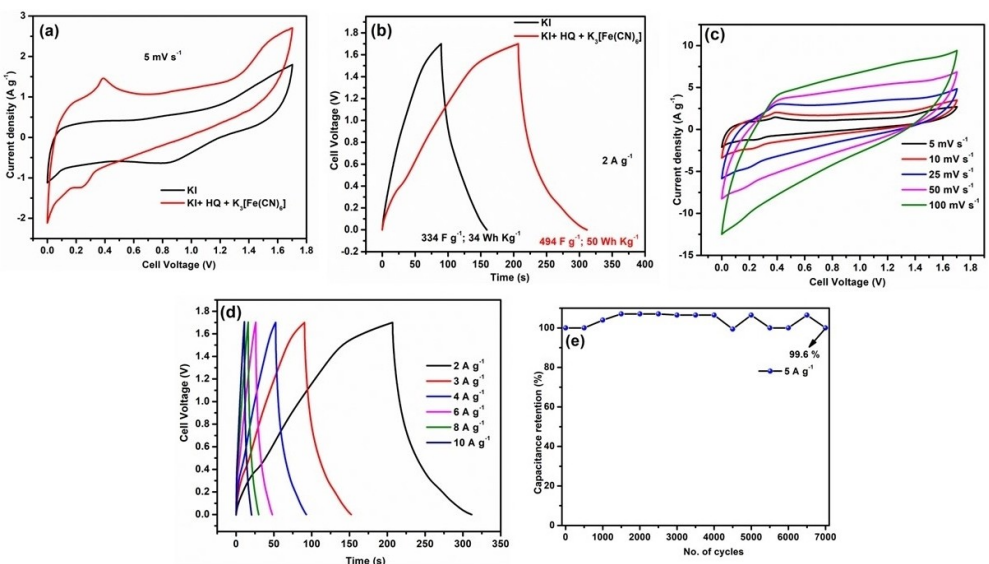


Figure 16. (a) CV and (b) GCD profile of the B1P3GO symmetric cell in $0.01 \text{ M KI-1 M H}_2\text{SO}_4$ and $0.01 \text{ M HQ-0.01 M KI-0.01 M K}_3[\text{Fe}(\text{CN})_6]/1 \text{ M H}_2\text{SO}_4$ solution at 5 mV s^{-1} and 2 A g^{-1} , (c) CV and (d) GCD profile of B1P3GO symmetric cell at different scan rates and current densities in $0.01 \text{ M HQ-0.01 M KI-0.01 M K}_3[\text{Fe}(\text{CN})_6]/1 \text{ M H}_2\text{SO}_4$ solution and (e) cycle-life profile for B1P3GO symmetric cell at 5 A g^{-1} over 7000 cycles, respectively.

Table 6. Specific capacitance, Energy density and Power density of symmetric B1P3GO cell in triple redox additives at different current densities.

Symmetric B1P3GO cell in triple redox additives			
Current density (A g ⁻¹)	C _{sp} (F g ⁻¹)	E (Wh Kg ⁻¹)	P (W Kg ⁻¹)
2	494	50	1696
3	431	43	2538
4	386	39	3424
6	311	31.2	5105
8	264	26.5	6814
10	219	22	8516

and 99.7% of retention in capacitance was achieved as shown in Figure 16e. The structural stability of the electrode after cycling has been studied by comparing the surface morphology of the electrode before and after stability studies. Figures S9a and b depict the SEM images of the electrode before and after cycling at 5 A g⁻¹ over 7000 cycles. From Figures S9a and b, it is more apparent that the electrode exhibits a flake-like structure and also there is no change in the morphology after stability studies. It was inferred that the fabricated electrode is structurally stable even after cycling over 7000 cycles at 5 A g⁻¹ in triple redox additives incorporated aqueous electrolyte. The gravimetric capacitance, energy, and power density for the symmetric B1P3GO cell in triple redox additives at varying current densities are tabulated in Table 6. The efficiency of any supercapacitor device is determined by two significant parameters: energy and coulombic efficiency. The expression for the calculation of the energy efficiency of any supercapacitor device is shown below.^[34]

$$\text{Energy efficiency} = \frac{(\text{Energy density})(\text{discharge})^*}{(\text{Energy density})(\text{charge})} \times 100$$

The energy efficiency of B1P3GO symmetric cell in triple redox additives calculated at different current densities such as 2, 3, 4, 6, 8 and 10 A/g are 51, 67, 80, 84, 87 and 85%, respectively. Similarly, the energy efficiency of the same cell in KI determined at different current densities such as 2, 3, 4, 6, 8 and 10 A/g are 77.6, 83, 85.6, 93, 89.4 and 93.6%, respectively. For 1 M H₂SO₄, the energy efficiency derived at different current densities such as 1, 2, 3, 4, 5, and 10 A/g are 97, 96, 92.4, 90.2, 85.7 and 69.3%, respectively. From this, it is strongly evident that the energy efficiency diminishes with the current density of the aqueous electrolyte while the energy efficiency enhances with the current density of the redox additive incorporated aqueous electrolyte.

The coulombic efficiency was calculated by using the following equation:^[72]

$$\eta = \left(\frac{\Delta t_d}{\Delta t_c} \right)^* \times 100$$

Where η is the coulombic efficiency (%), Δt_d and Δt_c are discharge time and charge time, respectively. The coulombic efficiencies calculated in KI/1 M H₂SO₄ at varying current densities such as 2, 3, 4, 6, 8 and 10 A g⁻¹ are found to be 76.6, 82.6, 85.7, 92.8, 88.8 and 93.3%, respectively. Similarly, coulombic efficiencies evaluated at 2, 3, 4, 6, 8 and 10 A g⁻¹ in triple redox additives are found to be 50.2, 67.3, 78.5, 84.6, 87 and 85.3%, respectively. From Figure 16b, it is strongly evident that the charging time in triple redox additives is significantly higher than that in single redox additives (KI). It has been anticipated that more redox processes will occur over the B1P3GO electrode with triple redox additive thereby utilizing more charging time leading to the decreased coulombic efficiency. Hence the coulombic efficiency of the B1P3GO symmetric cell in triple redox additive is appreciably lesser than in single redox additive.

Figure 17 shows the Ragone plot for the B1P3GO-based symmetric supercapacitor in 1 M H₂SO₄, 0.01 M KI-1 M H₂SO₄ and 0.01 M KI-0.01 M HQ-0.01 M K₃[Fe(CN)₆]/1 M H₂SO₄ solution. The calculated energy and power density at 1 A g⁻¹ in 1 M H₂SO₄ solution are found to be 6.4 Wh Kg⁻¹ and 501 W Kg⁻¹, respectively. However, at high current density (10 A g⁻¹), the energy density diminishes to 2.08 Wh Kg⁻¹ but the power density enhances to 4992 W Kg⁻¹. The energy density of the symmetric B1P3GO cell determined at 2 A g⁻¹ in 0.01 M KI-1 M H₂SO₄ and triple redox additive are found to be 33 Wh Kg⁻¹ and 50 Wh Kg⁻¹ which is appreciably superior to 1 M H₂SO₄ solution alone, respectively. Similarly, at enhanced current density (10 A g⁻¹), the calculated power density for the B1P3GO symmetric cell in 0.01 M KI-1 M H₂SO₄ and triple redox additive are found to be 8511 W Kg⁻¹ and 8516 W Kg⁻¹ and higher than 1 M H₂SO₄ solution (4999 W Kg⁻¹). The values of specific capacitance, energy density and power density for the B1P3GO symmetric cell in 1 M H₂SO₄, 0.01 M KI/1 M H₂SO₄ and triple redox additives are tabulated in Table S3, Table S4 and Table 6, respectively. The energy density obtained by the B1P3GO in both single and triple redox additives is compared with earlier reports and tabulated in Table 7. From Figure 17, it can be seen that the energy density of the B1P3GO symmetric cell in single and triple redox additives lies between batteries and supercapacitors but the energy density for the same cell in 1 M H₂SO₄ solution lie in between supercapacitor and capacitor. On the other hand, the power density in 1 M H₂SO₄ is preferably distributed in the supercapacitor region while that of the same cell in single as well as triple redox additives is preferentially found in the capacitor regime. Hence it was concluded that both energy as well as power density enriched upon the incorporation of more and more redox additives in aqueous electrolyte.

3. Conclusions

The electrochemical capacitive performance of B, P dual-doped graphene in aqueous as well as redox additive-based aqueous electrolytes are extensively demonstrated. Both the presence as well as the quantity of dual doping were scrutinized with EDAX

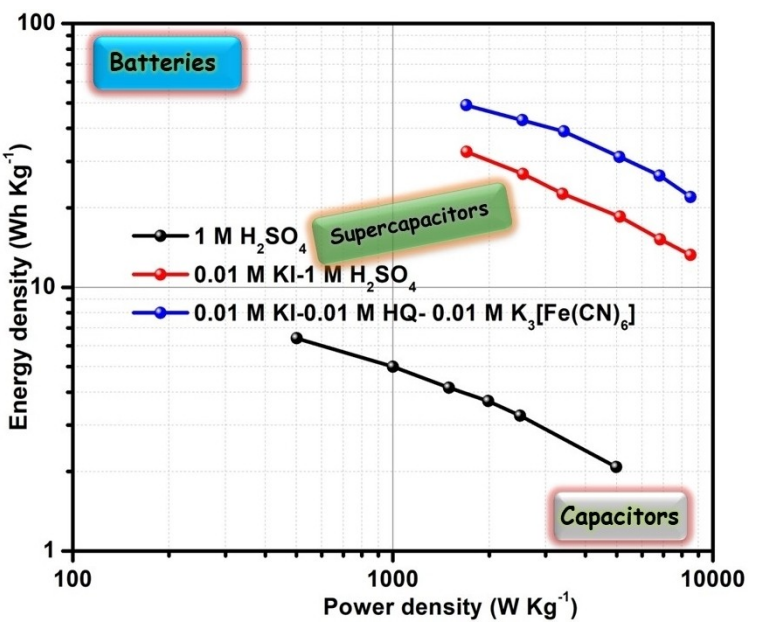


Figure 17. Ragone plot for the B1P3GO symmetric cell in 1 M H_2SO_4 , 0.01 M KI/1 M H_2SO_4 and triple redox additives.

and XPS techniques. Electrochemical experiments revealed that the B, P dual-doped graphene derived from the boron and phosphorus dopant are in weight ratio of 1:3 submitted the enriched gravimetric capacitance of 360 F g^{-1} in aqueous electrolyte (1 M H_2SO_4) at 1 A g^{-1} . Also, the gravimetric capacitance (F g^{-1}) at 3 A g^{-1} calculated for the B1P3GO electrode are 289 (1 M H_2SO_4) > 86 (1 M KOH) > 45 (1 M Na_2SO_4) suggesting that the nature of media played a crucial role for the capacitive performance. The symmetric supercapacitor

investigations demonstrated that the symmetric B1P3GO cell has attained the energy-increased density of 50 Wh Kg^{-1} along with 99% retention from its initial capacitance over 7000 cycles in the triple redox additives aided aqueous electrolyte $\text{KI}-\text{HQ}-\text{K}_3[\text{Fe}(\text{CN})_6]/1 \text{ M } \text{H}_2\text{SO}_4$. This value is found to be superior to KI/1 M H_2SO_4 (33 Wh Kg^{-1}) and 1 M H_2SO_4 solution (5 Wh Kg^{-1}). Hence the multiple redox additive mixtures are highly promising as well as more reliable for enhancing the energy density of carbon-based symmetric supercapacitors.

Table 7. Comparison table of energy density of B, P dual doped graphene in triple redox additives with various carbon-based symmetric supercapacitors in different redox additive based aqueous electrolytes.

Materials	Redox Additives	Energy density (Wh Kg^{-1})	Ref.
N-doped carbon	4-hydroxybenzoic acid + H_2SO_4	10.5	[73]
S-doped graphene	Hydroquinone + H_2SO_4	27	[74]
N-doped graphene	Na_2MoO_4 + H_2SO_4	23	[41]
Activated Carbon	VOSO_4 + H_2SO_4	13.7	[43]
Honeycomb like carbon	5, 6 dihydroxyindole + H_2SO_4	8.8	[75]
Activated Carbon	Na salt of calcon carboxylic acid + KOH	11	[76]
Biocarbon from Konjaku Fluor	p-phenylenediamine + KOH	9.2	[77]
N-rich nanoporous carbon	KBr + H_2SO_4	18.25	[78]
N, O dual doped porous carbon	KI + H_2SO_4	18	[79]
N, B dual doped Ordered mesoporous carbon	NH_4VO_3 + FeSO_4 + H_2SO_4	48.4	[49]
Active carbon	1 M KNO_3 + 0.1 M Anthraquinone-2,7-disulphonate (AQDS)	21.2	[80]
Biocarbon derived from pomelo peels	Na_2SO_4 —NaI—KI	22.75	[81]
2D Carbon sheets	HQ + DQ + H_2SO_4	21	[82]
	HQ + H_2SO_4	11.1	[82]
Se doped graphene	NH_4VO_3 + H_2SO_4	23	[83]
B, P dual-doped graphene	KI + HQ + $\text{K}_3[\text{Fe}(\text{CN})_6]$ + H_2SO_4	50	This work
	KI + H_2SO_4	33	

Acknowledgements

The author S. Suresh Balaji (No. F 4-2/2006 (BSR)/ CH/20-21/0196) thanks the University Grants Commission, New Delhi for the award of Dr. D. S. Kothari Postdoctoral Fellowship, and financial support. The authors thank the Sophisticated Analytical Instrumentation Facility (SAIF), and the Department of Chemistry IIT Madras, for HRSEM, FT-IR and XRD facilities. The author thanks Dept. of Medical Physics, Anna University for the Raman spectral facility. The authors also thank the Centre for Nanoscience and Nanotechnology, Sathyabama University, Chennai and CIF, CECRI (Karaikudi) for HRTEM and XPS characterization facilities, respectively. Also, the authors acknowledge Material Analysis & Research Centre, Bengaluru for the BET N₂ adsorption-desorption analysis and pore size measurements. The authors also acknowledge Prof. R. Jayavel, Dean, Alagappa College of Technology, Anna University for permitting to carry out electrochemical stability involving GCD and impedance spectroscopy investigations.

Conflict of Interests

The authors declare no conflict of interest.

Data Availability Statement

The data that support the findings of this study are available from the corresponding author upon reasonable request.

Keywords: B, P dual-doped graphene · Triple Redox additives · Supercapacitors · Charge storage · Energy density

- [1] P. Simon, Y. Gogotsi, *Nat. Mater.* **2008**, *7*, 845–854.
- [2] J. Yan, Q. Wang, T. Wei, Z. Fan, *Adv. Energy Mater.* **2014**, *4*, 1300816.
- [3] L. L. Zhang, R. Zhou, X. S. Zhao, *J. Mater. Chem.* **2010**, *20*, 5983–5992.
- [4] A. Velasco, Y. K. Ryu, A. Boscá, A. Ladrón-De-Guevara, E. Hunt, J. Zuo, J. Pedrós, F. Calle, J. Martínez, *Sustain. Energy Fuels* **2021**, *5*, 1235–1254.
- [5] L. Fekri Aval, M. Ghoranneviss, G. Behzadi Pour, *Heliyon* **2018**, *4*, e00862.
- [6] V. Kuzmenko, N. Wang, M. Haque, O. Naboka, M. Flygare, K. Svensson, P. Gatenholm, J. Liu, P. Enoksson, *RSC Adv.* **2017**, *7*, 45968–45977.
- [7] A. Daraghmeh, S. Hussain, I. Saadeddin, L. Servera, E. Xuriguera, A. Cornet, A. Cirera, *Nanoscale Res. Lett.* **2017**, *12*, 639.
- [8] S. Ahmed, A. Ahmed, M. Rafat, *J. Saudi Chem. Soc.* **2018**, *22*, 993–1002.
- [9] G. S. Jang, S. Ameen, M. S. Akhtar, H. S. Shin, *Ceram. Int.* **2018**, *44*, 588–595.
- [10] H. Yan, K. Zhu, X. Liu, Y. Wang, Y. Wang, D. Zhang, Y. Lu, T. Peng, Y. Liu, Y. Luo, *RSC Adv.* **2020**, *10*, 8760–8765.
- [11] X. Yi, H. Sun, N. Robertson, C. Kirk, *Sustain. Energy Fuels* **2021**, *5*, 5236–5246.
- [12] A. M. Kale, R. Manikandan, C. Justin Raj, A. Dennyson Savariraj, C. Voz, B. C. Kim, *Mater. Today Energy* **2021**, *21*, 100736.
- [13] M. Sathish, S. Mitani, T. Tomai, I. Honma, *J. Mater. Chem.* **2011**, *21*, 16216–16222.
- [14] R. Velayutham, R. Manikandan, C. Justin Raj, A. Dennyson Savariraj, W. J. Cho, H. M. Jang, B. Chul Kim, *Appl. Surf. Sci.* **2021**, *570*, 151051.
- [15] E. Bao, J. Sun, Y. Liu, X. Ren, X. Liu, C. Xu, H. Chen, *Int. J. Hydrogen Energy* **2022**, *47*, 39204–39214.
- [16] Y. Liu, X. Du, Y. Li, E. Bao, X. Ren, H. Chen, X. Tian, C. Xu, *J. Colloid Interface Sci.* **2022**, *627*, 815–826.
- [17] J. Sun, C. Xu, H. Chen, *J. Mater.* **2021**, *7*, 98–126.
- [18] X. Ren, Y. Liu, H. Sun, Z. Zhang, C. Luo, Y. Wang, C. Xu, H. Chen, *J. Energy Storage* **2023**, *74*, 109372.
- [19] E. Bao, X. Ren, Y. Wang, Z. Zhang, C. Luo, X. Liu, C. Xu, H. Chen, *J. Energy Storage* **2024**, *82*, 110535.
- [20] H. Sun, Y. Miao, G. Wang, X. Han, Y. Wang, Z. Zhang, C. Luo, X. Liu, C. Xu, H. Chen, *J. Energy Storage* **2024**, *76*, 109780.
- [21] Y. Gao, Y. Li, H. An, Y. Feng, W. Feng, *RSC Adv.* **2017**, *7*, 8762–8770.
- [22] N. Xiao, H. Tan, J. Zhu, L. Tan, X. Rui, X. Dong, Q. Yan, *ACS Appl. Mater. Interfaces* **2013**, *5*, 9656–9662.
- [23] Y. Wen, C. Huang, L. Wang, D. Hulicova-Jurcakova, *Chin. Sci. Bull.* **2014**, *59*, 2102–2121.
- [24] S. Ghosh, S. Barg, S. M. Jeong, K. Ostrrikov, *Adv. Energy Mater.* **2020**, *10*, 200129.
- [25] M. Khanda, C. Van Tran, J. Bin In, *Appl. Surf. Sci.* **2022**, *576*, 151714.
- [26] X. Yu, Y. Kang, H. S. Park, *Carbon* **2016**, *101*, 49–56.
- [27] D. Prakash, S. Manivannan, *Surf. Interfaces* **2021**, *23*, 101025.
- [28] W. Kong, J. Zhu, M. Zhang, Y. Liu, J. Hu, *Microporous Mesoporous Mater.* **2018**, *268*, 260–267.
- [29] W. Wang, W. Zhang, G. Wang, C. Li, *J. Mater. Chem. A* **2021**, *9*, 15766–15775.
- [30] G. Li, Y. Li, J. Deng, H. Lin, X. Hou, L. Jia, *Mater. Chem. Front.* **2020**, *4*, 2704–2715.
- [31] Y. Sim, S. J. Kim, G. Janani, Y. Chae, S. Surendran, H. Kim, S. Yoo, D. C. Seok, Y. H. Jung, C. Jeon, J. Moon, U. Sim, *Appl. Surf. Sci.* **2020**, *507*, 145157.
- [32] Y. Chen, Y. Li, F. Yao, C. Peng, C. Cao, Y. Feng, W. Feng, *Sustain. Energy Fuels* **2019**, *3*, 2237–2245.
- [33] M. Sandhiya, U. K. K. Veerappan, M. Sathish, *Chem. Commun.* **2021**, *57*, 8336–8339.
- [34] D. Johnsirani, A. Pandurangan, *Diamond Relat. Mater.* **2020**, *105*, 107800.
- [35] S. Sekar, P. Arumugam, G. Rajamanickam, *Fullerenes Nanotubes Carbon Nanostruct.* **2023**, 845–855.
- [36] P. M. Pandian, A. Pandurangan, *New J. Chem.* **2021**, *45*, 12408–12425.
- [37] E. Frackowiak, M. Meller, J. Menzel, D. Gastol, K. Fic, *Faraday Discuss.* **2014**, *172*, 179–198.
- [38] D. Jain, J. Kanungo, S. K. Tripathi, *Appl. Phys. A* **2018**, *124*, 397.
- [39] X. N. Sun, W. Hu, D. Xu, X. Y. Chen, P. Cui, *Ind. Eng. Chem. Res.* **2017**, *56*, 2433–2433.
- [40] K. Nasrin, S. Gokulnath, M. Karnan, K. Subramani, M. Sathish, *Energy Fuels* **2021**, *35*, 6465–6482.
- [41] M. Sandhiya, Vivekanand, S. Suresh Balaji, M. Sathish, *ACS Appl. Energ. Mater.* **2020**, *3*, 11368–11377.
- [42] M. Sandhiya, Vivekanand, S. Suresh Balaji, M. Sathish, *J. Phys. Chem. C* **2021**, *125*, 8068–8079.
- [43] S. T. Senthilkumar, R. K. Selvan, N. Ponpandian, J. S. Melo, Y. S. Lee, *J. Mater. Chem. A* **2013**, *1*, 7913–7919.
- [44] M. Moorthy, M. Karnan, S. Suresh Balaji, S. Gokulnath, M. Sathish, *J. Electroanal. Chem.* **2022**, *924*, 116857.
- [45] K. Manickavasakam, S. Suresh Balaji, S. Kaipannan, A. G. Karthick Raj, S. Veeman, S. Marappan, *J. Energy Storage* **2020**, *32*, 101939.
- [46] T. A. Raja, P. Vickraman, *Int. J. Energy Res.* **2022**, *46*, 9097–9113.
- [47] N. Yadav, S. A. Hashmi, *J. Mater. Chem. A* **2020**, *8*, 18266–18279.
- [48] D. Xu, W. Hu, X. N. Sun, P. Cui, X. Y. Chen, *J. Power Sources* **2017**, *341*, 448–456.
- [49] K. Subramani, S. Shunmugasundaram, V. Duraisamy, R. Ilavarasi, S. Murugesan Senthil Kumar, M. Sathish, *J. Colloid Interface Sci.* **2022**, *606*, 286–297.
- [50] S. Sathyamoorthy, M. Kanagaraj, M. Kathiresan, V. Suryanarayanan, D. Velayutham, *J. Mater. Chem. A* **2016**, *4*, 4562–4569.
- [51] Y. C. Chen, L. Y. Lin, *J. Colloid Interface Sci.* **2019**, *537*, 295–305.
- [52] H. Wang, T. Maiyalagan, X. Wang, *ACS Catal.* **2012**, *2*, 781–794.
- [53] J. Qi, W. Zhang, L. Xu, *Chem. Eur. J.* **2018**, *24*, 18097–18105.
- [54] S. S. Balaji, M. Karnan, J. Kamarsamam, M. Sathish, *ChemElectroChem* **2019**, *6*, 1492–1499.
- [55] S. S. Balaji, M. Karnan, P. Anandhaganesh, S. M. Tauquir, M. Sathish, *Appl. Surf. Sci.* **2019**, *491*, 560–569.
- [56] S. Suresh Balaji, S. Mohammad Tauquir, M. Karnan, M. Moorthy, M. Sathish, *ChemistrySelect* **2020**, *5*, 9825–9833.
- [57] V. Thirumal, A. Pandurangan, R. Jayavel, R. Ilangovalan, *Synth. Met.* **2016**, *220*, 524–532.
- [58] S. Suresh Balaji, M. Sandhiya, M. Sathish, *J. Energy Storage* **2021**, *33*, 102085.
- [59] V. Thirumal, A. Pandurangan, R. Jayavel, K. S. Venkatesh, N. S. Palani, R. Ragavan, R. Ilangovalan, *J. Mater. Sci. Mater. Electron.* **2015**, *26*, 6319–6328.

- [60] S. Dou, X. Huang, Z. Ma, J. Wu, S. Wang, *Nanotechnology* **2015**, *26*, 045402.
- [61] Y. Kang, B. Wang, Y. Yan, H. H. Rana, J. Y. Lee, J. H. Kim, H. S. Park, *Mater. Today Commun.* **2020**, *25*, 101495.
- [62] X. Du, W. Wang, M. Han, X. Guo, X. Shi, K. Cao, *ChemistrySelect* **2022**, *7*, e202202645.
- [63] L. B. Xing, S. F. Hou, J. L. Zhang, J. Zhou, Z. Li, W. Si, S. Zhuo, *Mater. Lett.* **2015**, *147*, 97–100.
- [64] M. Sandhiya, J. Power Sources **2022**, *540*, 231587.
- [65] D. Duan, F. Hu, J. Ma, H. Peng, K. Zhang, P. Huang, H. Chu, X. Lin, S. Qiu, S. Wei, F. Xu, L. Sun, *J. Mater. Sci. Mater. Electron.* **2019**, *30*, 19505–19512.
- [66] S. Xue, P. Zhang, B. Liu, J. Liu, Q. Yan, H. Pan, W. Tu, H. Zhang, *Int. J. Energy Res.* **2022**, *46*, 11400–11410.
- [67] J. Chen, C. Lin, M. Zhang, T. Jin, Y. Qian, *ChemElectroChem* **2020**, *7*, 3311–3318.
- [68] S. Suresh Balaji, M. Karnan, M. Sathish, *Int. J. Hydrogen Energy* **2018**, *43*, 4044–4057.
- [69] A. Singh, A. Chandra, *Sci. Rep.* **2016**, *6*, 25793.
- [70] K. H. Lee, J. Oh, J. G. Son, H. Kim, S.-S. Lee, *ACS Appl. Mater. Interfaces* **2014**, *6*, 6361–6368.
- [71] R. Karkuzhali, S. Manoj, K. Shanmugapriya, A. V. Narendra Kumar, G. Gopu, N. Muniyappan, B. H. Jeon, S. Muthu Prabhu, *J. Solid State Chem.* **2022**, *306*, 122727.
- [72] S. S. Balaji, A. Elavarasan, M. Sathish, *Electrochim. Acta* **2016**, *200*, 37–45.
- [73] W. Hu, D. Xu, X. N. Sun, Z. H. Xiao, X. Y. Chen, Z. J. Zhang, *ACS Sustainable Chem. Eng.* **2017**, *5*, 8630–8640.
- [74] M. Sandhiya, S. Suresh Balaji, M. Sathish, *Energy Fuels* **2020**, *34*, 11536–11546.
- [75] T. Xiong, W. S. V. Lee, L. Chen, T. L. Tan, X. Huang, J. Xue, *Energy Environ. Sci.* **2017**, *10*, 2441–2449.
- [76] Q. Wang, Y. F. Nie, Z. H. Xiao, X. Y. Chen, Z. J. Zhang, *J. Electroanal. Chem.* **2016**, *770*, 62–72.
- [77] X. Q. Lin, Q. F. Lü, Q. Li, M. Wu, R. Liu, *ACS Omega* **2018**, *3*, 13283–13289.
- [78] M. Mansuer, L. Miao, D. Zhu, H. Duan, Y. Lv, L. Li, M. Liu, L. Gan, *Mater. Chem. Front.* **2021**, *5*, 3061–3072.
- [79] Z. Zhou, L. Miao, H. Duan, Z. Wang, Y. Lv, W. Xiong, D. Zhu, L. Li, M. Liu, L. Gan, *Chin. Chem. Lett.* **2020**, *31*, 1226–1230.
- [80] Y. Tian, R. Xue, X. Zhou, Z. Liu, L. Huang, *Electrochim. Acta* **2015**, *152*, 135–139.
- [81] N. T. Nguyen, P. A. Le, V. B. T. Phung, *J. Nanopart. Res.* **2020**, *22*.
- [82] D. Xu, X. N. Sun, W. Hu, X. Y. Chen, *J. Power Sources* **2017**, *357*, 107–116.
- [83] Vivekanand, S.S. Balaji, K. Nasrin, M. Sathish, *ChemNanoMat* **2023**, *9*, e202300209.

Manuscript received: January 13, 2024

Revised manuscript received: March 30, 2024

Accepted manuscript online: April 12, 2024

Version of record online: May 13, 2024